AGU100 ADVANCING EARTH AND SPACE SCIENCE

JGR

Journal of Geophysical Research: Solid Earth

RESEARCH ARTICLE
10.1029/2017JB015421

Key Points:
- This is the first study presenting 3-D kernels of Rayleigh wave ZH amplitude ratios based on full-wave finite frequency theory
- The 3-D full-wave ZH ratio kernels vary with back azimuths and are significant within one wavelength distance of the receiver
- The 3-D full-wave ZH ratio and other component-differential kernels provide a tool to precisely image Earth structures beneath a dense array

Supporting Information:
- Supporting Information S1

Correspondence to:
X. Bao,
xybao@uri.edu

Citation:
Bao, X., & Shen, Y. (2018). Full-waveform sensitivity kernels of component-differential traveltimes and ZH amplitude ratios for velocity and density tomography. *Journal of Geophysical Research: Solid Earth*, *123*. https://doi.org/10.1029/2017JB015421

Received 29 DEC 2017
Accepted 17 MAY 2018
Accepted article online 24 MAY 2018

Full-Waveform Sensitivity Kernels of Component-Differential Traveltimes and ZH Amplitude Ratios for Velocity and Density Tomography

Xueyang Bao[1] and Yang Shen[1]

[1]Graduate School of Oceanography, University of Rhode Island, Narragansett, RI, USA

Abstract Previous studies of the Rayleigh wave vertical-to-horizontal amplitude ratios (ZH ratio) assumed one-dimensional velocity and density structures beneath the receiver, neglecting the effects of three-dimensional (3-D) heterogeneities on wave amplitudes. Those studies have well demonstrated that the ZH ratios provide powerful constraints on the crust and mantle structure. However, the azimuthal averaging of the ZH ratios common in those studies means reduced sensitivities to the 3-D structure and thus the ZH ratios' potential resolving power. We derive equations for the 3-D full-wave sensitivity kernels of the ZH ratio and differential traveltime of the vertical and radial components of Rayleigh and *P* waves, to perturbations in shear and compressional velocities and density. The kernels are calculated based on finite difference modeling of wave propagation in 3-D structures and the scattering-integral method. We verify the 3-D full-wave sensitivity kernels by comparing the predictions from the kernels with the measurements from numerical simulations of wave propagation in models with various small-scale perturbations. In contrast to the 1-D depth sensitivity kernels, our 3-D full-wave kernels exhibit patterns that vary with back azimuths and distances within one wavelength of the receiver, indicating the resolving power not only vertically, and also laterally. In places with dense seismic stations, these kernels will provide a powerful tool to obtain accurate and high-resolution velocity and density models.

1. Introduction

The Rayleigh wave vertical-to-radial amplitude ratio (hereinafter ZH ratio, also known as Rayleigh wave ellipticity, or H/V ratio as its inverse) primarily reflects structures near seismic stations (Boore & Toksöz, 1969). Because its sensitivity to the velocity structure peaks at shallower depths than that of the Rayleigh wave phase velocity of a given period, the ZH ratio provides complementary constraints on the velocity structure. The ZH ratio has been used to determine the crust and mantle structures at various geographic scales (e.g., Attanayake et al., 2017; Li et al., 2016; Muir & Tsai, 2017; Yano et al., 2009). Chong et al. (2015, 2016) and Yuan et al. (2016) showed the benefits of joint inversion of ZH ratios and receiver functions or phase velocity dispersion for the velocity structure beneath stations. To date, most of the ZH ratio studies focused on inversions for shear-wave velocity V_s, though several have taken advantage of the fact that the ZH ratio is also sensitive to density ρ (and to a lesser extent, compressional wave velocity V_p) and can be used to constrain the density structure (e.g., Berbellini et al., 2017; Lin et al., 2012, 2014; Tanimoto & Alvizuri, 2006). In addition, ZH ratios do not depend on accurate instrument timing as traditional traveltimes do and thus can be particularly useful for data recorded by ocean-bottom seismometers, for which timing can sometimes be inaccurate due to nonlinear clock drift (e.g., Gouédard et al., 2014; Hannemann et al., 2014).

There are two common assumptions in the previous studies using ZH ratios. One is that the structure beneath the receiver is one-dimensional (1-D; e.g., Lin et al., 2012). The calculation of the 1-D ZH ratio kernels generally follows the numerical method presented by Tanimoto and Alvizuri (2006) or the analytical method of Tanimoto and Tsuboi (2009). The laterally homogeneous assumption neglects the effects of 3-D heterogeneities near the receiver on wave amplitudes, which may be responsible for large apparent scatters in ZH ratio measurements. Ferreira and Woodhouse (2007) reported substantial variability in Rayleigh wave ellipticity measurements and attributed it to small-scale structures in the Earth. Tanimoto and Rivera (2008) also noted large scatters in the ZH measurements and showed that stable estimates can be obtained after averaging the measurements for many earthquakes. The back azimuthal averaging of the ZH ratio (Berbellini et al., 2017; Tanimoto & Rivera, 2008) smoothens out its sensitivity

10.1029/2017JB015421

to small-scale structures, making it more compatible with the 1-D sensitivity kernels. On the other hand, this treatment dampens the sensitivity of the ZH ratio to the 3-D structure and thus reduces its potential resolving power. The second assumption in the conventional method is that ZH ratio measurements reflect pure fundamental-mode Rayleigh waves, which is not always true. For example, the mode conversion of wave propagation in 3-D structures may result in significant interference of *S* and Love waves in Rayleigh wave polarization (Tanimoto et al., 2013). In addition, some combination of source depth and focal mechanism may lead to a high ratio of higher-mode to fundamental-mode Rayleigh wave energy (Fichtner, 2011).

Using Green's functions for incoming plane waves in 1-D structures (Liu & Zhou, 2016; Zhou et al., 2004) in a flat Cartesian/cylindrical coordinate system, Maupin (2017) calculated 3-D sensitivity kernels of ZH ratios, which show complex patterns with the maximum sensitivity close to the station. However, the azimuthally averaged 3-D kernels do not match the 1-D kernel. Maupin (2017) did not find an explanation for the discrepancy but suggested that a possible extension of her work would be to allow for a laterally heterogeneous background instead of a laterally homogeneous one. Indeed, as deployment of dense seismic arrays becomes a common practice, it is increasingly desirable to understand how small-scale heterogeneities beneath and near the receivers affect wave polarization. Such understanding, in the form of full-wave finite frequency Fréchet kernels based on a 3-D heterogeneous reference model will allow us to use the ZH ratios to better image 3-D velocity and density structures.

Similar to ZH ratios, the differential traveltime between the vertical and radial components (hereinafter component-differential traveltime) also provide constraints on near-receiver structure. While Rayleigh wave ZH ratios have been used in seismic tomography, the ZH component difference in traveltimes and amplitudes of body waves has not been applied yet, to the best of our knowledge. Shen et al. (2008) showed the component-differential traveltime and amplitude kernels of body waves to only velocity perturbations. In this paper, we calculate the first full-wave 3-D sensitivity kernels of Rayleigh and *P* wave ZH ratios and component-differential traveltimes to V_s, V_p, and ρ perturbations. We verify the kernels by comparing the predictions from the kernels with measurements from numerical simulations of wave propagation in models with various small-scale perturbations. We also compare our 3-D full-wave kernels with traditional 1-D kernels and suggest that our full-wave 3-D kernels can be used to achieve high-resolution 3-D velocity and density tomographic models beneath seismic arrays.

2. Method

We first briefly review the traveltime and amplitude sensitivity kernels for single-component seismograms and then introduce the kernels for differential phase delays and amplitude ratios of the vertical and horizontal components.

Following the full-waveform finite frequency theory, when the V_p, V_s, and ρ are selected as independent parameters, the perturbations in *P* and *S* wave velocity δV_P and δV_s, and density $\delta\rho$ are typically inverted using phase delay measurements, δt:

$$\delta t = \int\left[K^p_{V_p}(\boldsymbol{r})\delta V_p + K^p_{V_s}(\boldsymbol{r})\delta V_s + K^p_{\rho}(\boldsymbol{r})\delta\rho\right]dV. \tag{1}$$

where $K^p_{V_p}$, $K^p_{V_s}$, and K^p_{ρ} are the traveltime sensitivity kernels to V_p, V_s, and ρ perturbations (Fichtner, 2011; Tromp et al., 2005). Following the scattering-integral method (Chen et al., 2007; Shen et al., 2008; Zhang & Shen, 2008; Zhao et al., 2005), a small traveltime anomaly can be described as

$$\delta t = -\frac{\int_{t_1}^{t_2}\dot{\tilde{u}}(t)\delta u(t)dt}{\int_{t_1}^{t_2}\left|\dot{\tilde{u}}(t)\right|^2 dt}, \tag{2}$$

where $\delta u(t)$ is the perturbation of the displacement waveform, $u(t) - \tilde{u}(t)$; a tilde represents synthetics based on the reference model; a dot represents the time derivative; and t_1 and t_2 are the upper and lower limits of a finite time window. The traveltime anomaly δt equals the lag time at the maximum of the cross correlogram between the observed (perturbed) and synthetic (reference) waveforms. The corresponding traveltime sensitivities to δV_p, δV_s, and $\delta\rho$ are

10.1029/2017JB015421

$$K^{p}_{V_p}(\boldsymbol{r}) = -\frac{1}{\int_{t_1}^{t_2}\left|\dot{\widetilde{u}}_l(t)\right|^2 dt}\int_{t_1}^{t_2} 2\widetilde{\rho}\widetilde{V}_p\dot{\widetilde{u}}_l(\boldsymbol{r}_R,t;\boldsymbol{r}_S)\int_{-\infty}^{\infty}\widetilde{\boldsymbol{e}}_l\cdot\left[\left(\nabla\cdot\widetilde{\boldsymbol{G}}^T(\boldsymbol{r},\tau;\boldsymbol{r}_R)\right)(\nabla\cdot\widetilde{\boldsymbol{u}}(\boldsymbol{r},t-\tau;\boldsymbol{r}_S))\right]d\tau dt, \tag{3}$$

$$\begin{aligned} K^{p}_{V_s}(\boldsymbol{r}) = -\frac{1}{\int_{t_1}^{t_2}\left|\dot{\widetilde{u}}_l(t)\right|^2 dt}\int_{t_1}^{t_2} 2\widetilde{\rho}\widetilde{V}_s\dot{\widetilde{u}}_l(\boldsymbol{r}_R,t;\boldsymbol{r}_S)\int_{-\infty}^{\infty}\widetilde{\boldsymbol{e}}_l\cdot\Big\{\left(\nabla\widetilde{\boldsymbol{G}}(\boldsymbol{r},\tau;\boldsymbol{r}_R)\right)^{213} : [(\nabla\widetilde{\boldsymbol{u}}(\boldsymbol{r},t-\tau;\boldsymbol{r}_S)) \\ +(\nabla\widetilde{\boldsymbol{u}}(\boldsymbol{r},t-\tau;\boldsymbol{r}_S))^T\Big] - 2\left(\nabla\cdot\widetilde{\boldsymbol{G}}^T(\boldsymbol{r},\tau;\boldsymbol{r}_R)\right)(\nabla\cdot\widetilde{\boldsymbol{u}}(\boldsymbol{r},t-\tau;\boldsymbol{r}_S))\Big\}d\tau dt, \end{aligned} \tag{4}$$

and

$$K^{p}_{\rho}(\boldsymbol{r}) = \frac{1}{2}\left(K^{p}_{V_p}+K^{p}_{V_s}\right) - \frac{1}{\int_{t_1}^{t_2}\left|\dot{\widetilde{u}}_l(t)\right|^2 dt}\int_{t_1}^{t_2}\widetilde{\rho}\dot{\widetilde{u}}_l(\boldsymbol{r}_R,t;\boldsymbol{r}_S)\int_{-\infty}^{\infty}\widetilde{\boldsymbol{e}}_l\cdot\left[\left(\dot{\widetilde{\boldsymbol{u}}}(\boldsymbol{r},\tau;\boldsymbol{r}_R)\right)\cdot\left(\dot{\widetilde{\boldsymbol{u}}}(\boldsymbol{r},t-\tau;\boldsymbol{r}_S)\right)\right]d\tau dt. \tag{5}$$

Here $\boldsymbol{r}_S$ and $\boldsymbol{r}_R$ are the locations of the source and receiver, respectively; $\widetilde{\boldsymbol{e}}_l$ is the polarization direction; $\widetilde{\boldsymbol{G}}$ is the Green's tensor; and the symbol $()^{213}$ represents the transposition of the first and second indices of a third-order tensor. Equations (3) and (4) follow the formula by Zhang and Shen (2008) and Shen et al. (2008), which corrected a typo in Zhao et al. (2005). Two types of forward simulations are required to calculate the sensitivity kernels: one is to calculate the displacement field $\widetilde{\boldsymbol{u}}(\boldsymbol{r},t;\boldsymbol{r}_S)$ from the source $\boldsymbol{r}_s$ to location $\boldsymbol{r}$ and the velocity seismogram $\dot{\widetilde{u}}_l(\boldsymbol{r}_R,t;\boldsymbol{r}_S)$ from the source $\boldsymbol{r}_s$ to the receiver $\boldsymbol{r}_R$ and the second is to calculate the Green's tensor $\widetilde{\boldsymbol{G}}(\boldsymbol{r},\tau;\boldsymbol{r}_R)$ from the receiver $\boldsymbol{r}_R$ to location $\boldsymbol{r}$. The principle of reciprocity (Aki & Richards, 1980), $\widetilde{\boldsymbol{G}}(\boldsymbol{r},\tau;\boldsymbol{r}_R)=\widetilde{\boldsymbol{G}}(\boldsymbol{r}_R,\tau;\boldsymbol{r})$, has been applied to (3) and (4).

Similarly, the natural logarithm of the amplitude reduction can be defined as

$$\delta\ln A = -\frac{\int_{t_1}^{t_2}\widetilde{u}(t)\delta u(t)dt}{\int_{t_1}^{t_2}|\widetilde{u}(t)|^2 dt} = -\int\left[K^{q}_{V_p}(\boldsymbol{r})\delta V_p + K^{q}_{V_s}(\boldsymbol{r})\delta V_s + K^{q}_{\rho}(\boldsymbol{r})\delta\rho\right]dV. \tag{6}$$

Here A is the ratio between (i) the amplitude of the cross-correlogram of observed and synthetic waveforms at the lag time δt and (ii) the maximum amplitude of the auto-correlogram of the synthetic waveform (Ritsema et al., 2002; Tromp et al., 2005). The amplitude reduction sensitivity kernels to δV_p, δV_s, and $\delta\rho$ are

$$K^{q}_{V_p}(\boldsymbol{r}) = -\frac{1}{\int_{t_1}^{t_2}|\widetilde{u}_l(t)|^2 dt}\int_{t_1}^{t_2} 2\widetilde{\rho}\widetilde{V}_p\widetilde{u}_l(\boldsymbol{r}_R,t;\boldsymbol{r}_S)\int_{-\infty}^{\infty}\widetilde{\boldsymbol{e}}_l\cdot\left[\left(\nabla\cdot\widetilde{\boldsymbol{G}}^T(\boldsymbol{r},\tau;\boldsymbol{r}_R)\right)(\nabla\cdot\widetilde{\boldsymbol{u}}(\boldsymbol{r},t-\tau;\boldsymbol{r}_S))\right]d\tau dt, \tag{7}$$

$$\begin{aligned} K^{q}_{V_s}(\boldsymbol{r}) = -\frac{1}{\int_{t_1}^{t_2}|\widetilde{u}_l(t)|^2 dt}\int_{t_1}^{t_2} 2\widetilde{\rho}\widetilde{V}_s\widetilde{u}_l(\boldsymbol{r}_R,t;\boldsymbol{r}_S)\int_{-\infty}^{\infty}\widetilde{\boldsymbol{e}}_l\cdot\Big\{\left(\nabla\widetilde{\boldsymbol{G}}(\boldsymbol{r},\tau;\boldsymbol{r}_R)\right)^{213} : [(\nabla\widetilde{\boldsymbol{u}}(\boldsymbol{r},t-\tau;\boldsymbol{r}_S)) \\ +(\nabla\widetilde{\boldsymbol{u}}(\boldsymbol{r},t-\tau;\boldsymbol{r}_S))^T\Big] - 2\left(\nabla\cdot\widetilde{\boldsymbol{G}}^T(\boldsymbol{r},\tau;\boldsymbol{r}_R)\right)(\nabla\cdot\widetilde{\boldsymbol{u}}(\boldsymbol{r},t-\tau;\boldsymbol{r}_S))\Big\}d\tau dt. \end{aligned} \tag{8}$$

and

$$K^{q}_{\rho}(\boldsymbol{r}) = \frac{1}{2}\left(K^{q}_{V_p}+K^{q}_{V_s}\right) - \frac{1}{\int_{t_1}^{t_2}|\widetilde{u}_l(t)|^2 dt}\int_{t_1}^{t_2}\widetilde{\rho}\widetilde{u}_l(\boldsymbol{r}_R,t;\boldsymbol{r}_S)\int_{-\infty}^{\infty}\widetilde{\boldsymbol{e}}_l\cdot\left[\left(\dot{\widetilde{\boldsymbol{u}}}(\boldsymbol{r},\tau;\boldsymbol{r}_R)\right)\cdot\left(\dot{\widetilde{\boldsymbol{u}}}(\boldsymbol{r},t-\tau;\boldsymbol{r}_S)\right)\right]d\tau dt. \tag{9}$$

The differential traveltime between the vertical and radial components is thus described as

$$\delta t^Z - \delta t^R = -\frac{\int\dot{\widetilde{u}}^Z(t)\delta u^Z(t)dt}{\int\left[\dot{\widetilde{u}}^Z(t)\right]^2 dt} + \frac{\int\dot{\widetilde{u}}^R(t)\delta u^R(t)dt}{\int\left[\dot{\widetilde{u}}^R(t)\right]^2 dt} = \int\left[\left(K^{pZ}_{V_p}-K^{pR}_{V_p}\right)\delta V_p + \left(K^{pZ}_{V_s}-K^{pR}_{V_s}\right)\delta V_s + \left(K^{pZ}_{\rho}-K^{pR}_{\rho}\right)\delta\rho\right]dV, \tag{10}$$

where superscripts Z and R stand for the vertical and radial components, respectively. Similarly, the natural logarithm of the ratio of amplitude reduction on the vertical and radial components (hereinafter simply called ZH ratio) can be described as

10.1029/2017JB015421

$$\delta\ln\left(A^Z/A^R\right) = \delta\left(\ln A^Z - \ln A^R\right) = -\frac{\int \tilde{u}^Z(t)\delta u^Z(t)\mathrm{d}t}{\int\left[\tilde{u}^Z(t)\right]^2\mathrm{d}t} + \frac{\int \tilde{u}^R(t)\delta u^R(t)\mathrm{d}t}{\int\left[\tilde{u}^R(t)\right]^2\mathrm{d}t}$$
$$= -\int\left[\left(K_{V_p}^{qZ} - K_{V_p}^{qR}\right)\delta V_p + \left(K_{V_s}^{qZ} - K_{V_s}^{qR}\right)\delta V_s + \left(K_{\rho}^{qZ} - K_{\rho}^{qR}\right)\delta\rho\right]\mathrm{d}V. \quad (11)$$

Maupin (2017) calculated the ZH ratio kernels with a similar simple subtraction between the amplitude kernels of the radial and vertical components. We note that the ZH ratio in this study is based on waveforms in finite time windows according to the full-waveform finite frequency theory, which is different from the single-frequency single-mode ZH ratio defined in Tanimoto and Rivera (2008).

We calculate the sensitivity kernels using a 3-D finite-difference method in the spherical coordinates (Zhang et al., 2012). In the following examples, the computation is carried out for a 5.8° (longitude, from −1.4° to 4.4°) by 4.8° (latitude, from −2.4° to 2.4°) area with a vertical dimension from the Earth surface to 150 km depth. We place the source at the latitude and longitude of (0°, 0°) and depth of 12.315 km, and the receiver at (0°, 3°) on the Earth surface. The horizontal spacing of the finite difference grids is 0.01°, and the vertical grid spacing is variable, from 0.37 km near the surface to 1.77 km at the bottom of the model. This grid spacing is sufficient to accurately simulate surface waves at periods above ~5 s (Zhang et al., 2012). The time interval in simulation is 0.06 s to satisfy numerical stability. We use an explosive moment tensor at the source location, with a source time function of a 1.2-s-long bell integral, to calculate the forward wavefield, and a single force pulse at the receiver location approximated with a 1.2-s-long bell time function to calculate the backward wavefield and strain Green's tensor (Zhang & Shen, 2008). For simplicity and to minimize possible interference of other arrivals on Rayleigh waves, V_p, V_s, and ρ are all set as constant in the model (V_p = 6.3 km/s, V_s = 3.5 km/s, ρ = 2.8 kg/m^3). In section 4.2, we discuss the effect of laterally inhomogeneous model on the kernels.

3. Results

To illustrate the 3-D nature of the sensitivity kernels, we present several images of the traveltime and amplitude kernels for the model described above. Figure 1 shows the single-component ($K_{V_s}^{pZ}$, $K_{V_s}^{pR}, K_{V_s}^{qZ}, K_{V_s}^{qR}$) and component-differential $\left(K_{V_s}^{pZ} - K_{V_s}^{pR}, K_{V_s}^{qZ} - K_{V_s}^{qR}\right)$ traveltime and amplitude sensitivities to δV_s on a horizontal profile and the great-circle path vertical profile, for a time window that mainly includes Rayleigh waves of 10- to 20-s periods. Correspondingly, Figures 2 and 3 show the single-component sensitivity kernels for δV_p and $\delta\rho$ ($K_{V_p}^{pZ}$, $K_{V_p}^{pR}$, K_{ρ}^{pZ}, K_{ρ}^{pR}, $K_{V_p}^{qZ}$, $K_{V_p}^{qR}$, K_{ρ}^{qZ}) and their differential kernels ($K_{V_p}^{pZ} - K_{V_p}^{pR}$, $K_{\rho}^{pZ} - K_{\rho}^{pR}$, $K_{V_p}^{qZ} - K_{V_p}^{qR}$, $K_{\rho}^{qZ} - K_{\rho}^{qR}$).

The differential kernels vary with back azimuth and distance to the receiver, as well as with depth, indicating their resolving powers not only in depth, and also in lateral directions. In contrast, the 1-D kernels used in previous ZH ratio studies only have sensitivities in the vertical direction. We note that one common pattern in the ZH ratio and component-differential traveltime kernels is that the sensitivity is significant only near the receiver, over an area with a lateral dimension of approximately one wavelength (~50 km for Rayleigh waves with 10- to 20-s periods). This is clearly exhibited in the vertical profiles across and perpendicular to the great circle path at the receiver (Figure 4). In practice, this property can be used to reduce the computational cost in inversion of the component-differential traveltimes and ZH ratios, as we only need to calculate the differential kernels near the receiver.

We show in Figures S1–S3 in the supporting information the sensitivity kernels to δV_s, δV_p, and $\delta\rho$ for *P* waves at 10- to 20-s period. As for Rayleigh waves, the general pattern of the *P* wave differential kernels is that the sensitivity is significant near the receiver and negligible near the source and along most of the propagation path. The strong sensitivity to V_s observed here indicates the near-field effects at the receiver and significant *P*-to-*S* conversion at the free surface, which is consistent with the conclusion of Zhang and Shen (2008).

4. Discussion

4.1. Verification of the Kernels

We verify the single-component and component-differential kernels by running a series of numerical tests for a perturbed model with a rectangular prism perturbation of 1% centered at the latitude and longitude of (0°, 2.8°), approximately 20 km from the receiver along the great-circle path, to the otherwise constant V_p, V_s, and ρ. The

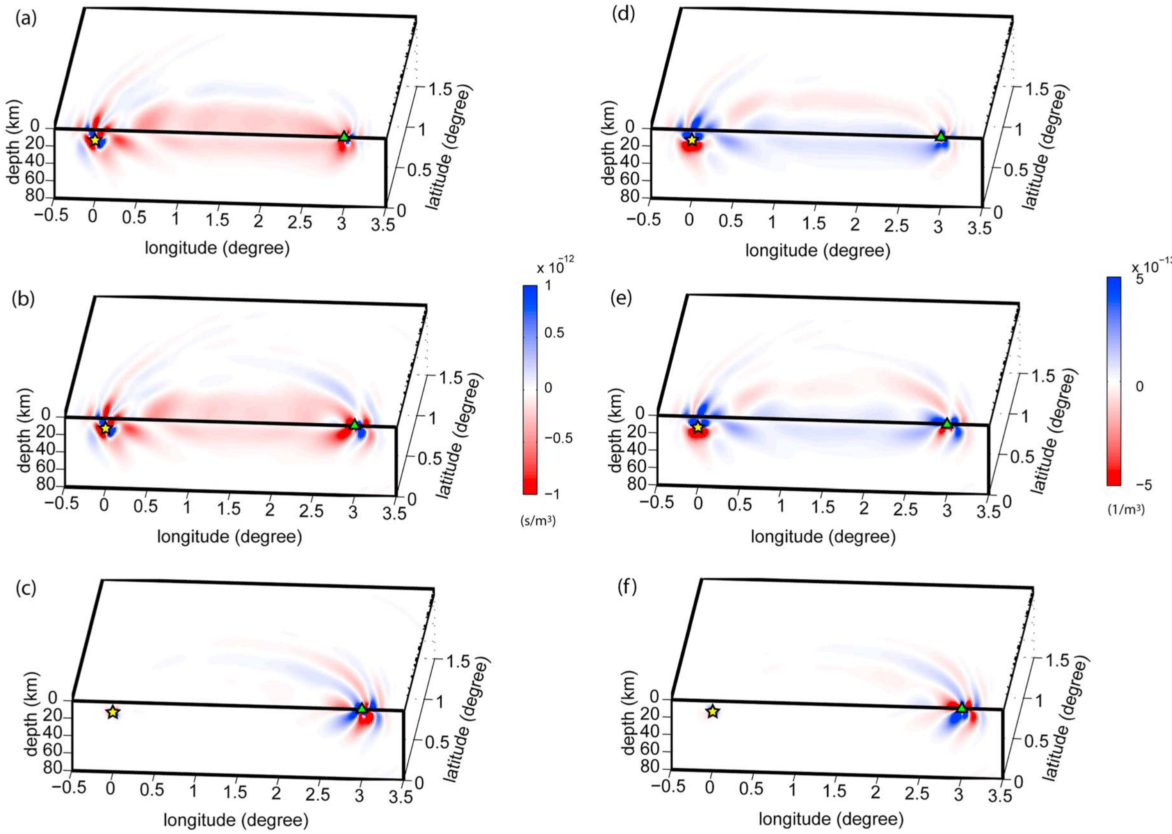

Figure 1. The 3-D view of the sensitivity kernels to V_s perturbations for Rayleigh waves at periods of 10–20 s, for (a) vertical-component traveltime, (b) radial-component traveltime, (c) vertical-radial differential traveltime; (d) vertical-component amplitude reduction, (e) radial-component amplitude reduction, and (f) ZH amplitude ratio. Yellow pentagrams and green triangles denote the source and receiver locations, respectively.

anomaly has a full width of 0.2° and a full height of 5 grids and is placed at various depths in the model. Since the vertical grid spacing increases with depths, the actual height of the anomaly increases from 1.56 km to 4.49 km with the central depth increases from 1.9 km to 36.4 km. An example of the model where ρ is perturbed but V_p and V_s remain unchanged is shown in Figure S4, indicating the independence of the model parameters. The kernels of the unperturbed model are used to calculate the "predicted" phase delay and amplitude reduction by the volume integration of the product of the kernel and perturbation. The synthetic seismograms from the reference and perturbed models are interpolated using a time step of 0.0001 s and compared by cross correlation at periods of 10–20 s, which yields the "measured" phase delay and amplitude reduction.

The "predicted" and "measured" component-differential phase delays and ZH ratios of Rayleigh and P waves are compared in Figures 5. The corresponding comparison for single components is shown in Figures S5 and S6. Overall, the kernel predictions match the measurements of the differential observables from direct cross-correlation well, verifying the component-differential sensitivity kernels of both Rayleigh and P waves. There are notable discrepancies between the predicted and measured amplitude reductions for single components (Figures S5 and S6). The discrepancies likely come from two sources: numerical errors and theoretical approximation. Using a smaller time interval in wave simulation, we estimate that the error due to the finite time interval and resampling of the synthetic seismograms is on the order of 5×10^{-4} s in traveltimes and 1×10^{-4} in amplitude reductions, at the same magnitude as most of the observed discrepancies. Another source of numerical error comes from the discretization of the input anomaly and the kernels on the finite difference grid, though this source of error yields about 1×10^{-4} s in traveltimes and 1×10^{-4} in amplitude reductions. These two sources of numerical errors might not fully explain some particularly large discrepancies of the amplitude reductions on single components (e.g., 8×10^{-4} at 10-km depth, Figure S5, top right).

10.1029/2017JB015421

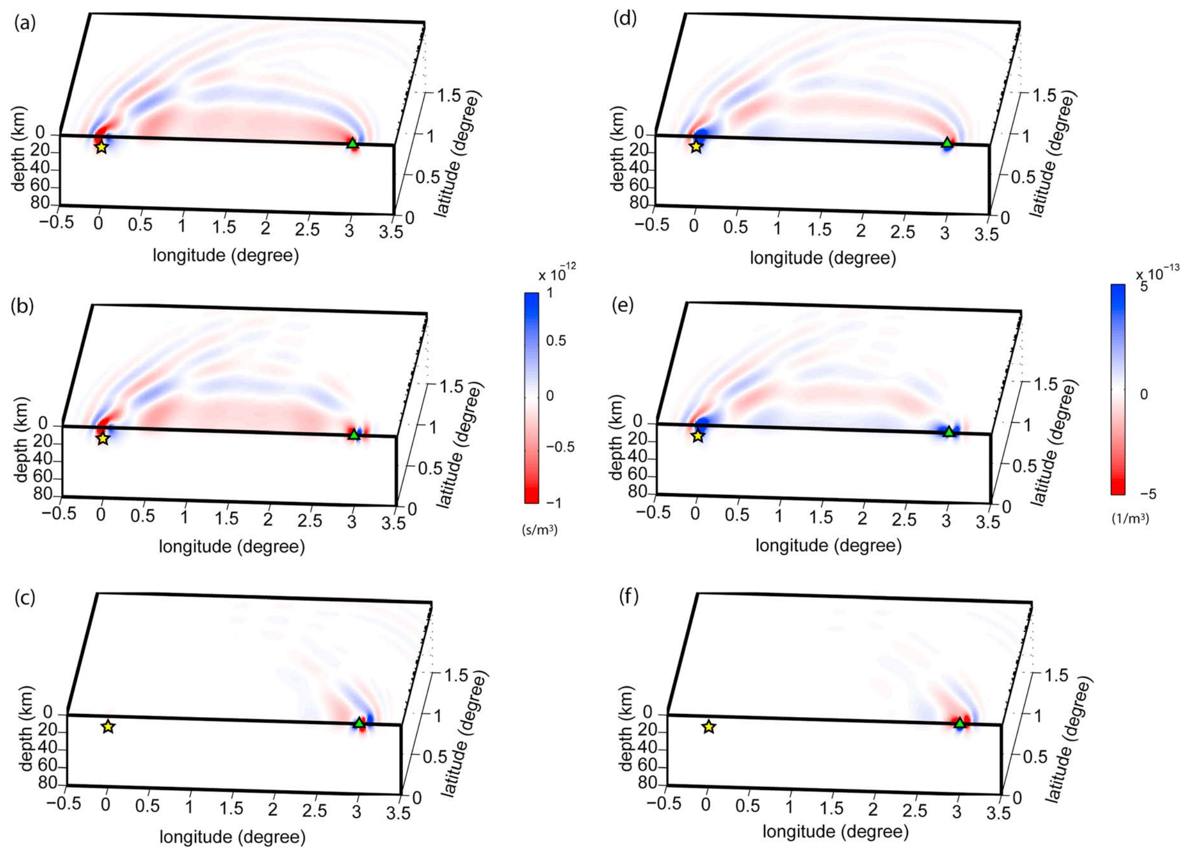

Figure 2. Same as Figure 1 except for the kernels to V_p.

A possible reason is that the current theory based on the Born approximation (Tromp et al., 2005; Zhang & Shen, 2008; Zhao et al., 2005) does not fully represent the effect of scattering on the waveform amplitudes. We note that the discrepancies on single components are to some extent canceled when we compare the ZH ratios (Figure 5), suggesting that the numerical errors and theoretical approximation affect the two components similarly. Thus, the use of component-differential observables removes or reduces not only the observational errors in the source (origin time, epicenter location, and source mechanism) and most of the propagation path but also prediction errors in computation and theoretical approximation, making it possible to achieve more accurate inversion results for structures near the receiver than using single-component observables.

4.2. 3-D Full-Wave Kernels Versus 1-D Kernels

Our full-waveform numerical approach overcomes the two issues in the previous Rayleigh wave ZH ratio studies. First, the 3-D sensitivity kernels obtained from full-waveform simulations provide more accurate accounts of the finite-frequency propagation effects in 3-D Earth models. Second, it is not required to separate the fundamental-mode Rayleigh waves and Rayleigh wave overtones or Love waves, since 3-D sensitivity kernels can be calculated for any arrival in any time window of a seismogram. Nevertheless, it may be informative to compare our 3-D full-wave kernels with the single-frequency fundamental-mode 1-D depth sensitivity kernels of Rayleigh wave ZH ratios used by previous studies.

In order to make the comparison, we reduce the spatial dimension of the ZH ratio kernels shown in Figures 1–3 from 3-D to 1-D, by summing the values on the horizontal plane at each vertical grid and plot them as a function of depth (Figure 6). These reduced 3-D kernels and the corresponding 1-D ZH ratio kernels (calculated using the code by Yuan et al., 2016) match well. The small differences between the reduced 3-D and the 1-D kernels can be attributed to two sources. One is the single period (15 s) in the 1-D kernels and a finite period range (10–20 s) in the calculation of the 3-D kernels. A comparison of the reduced 3-D kernels with the 1-D kernels at multiple

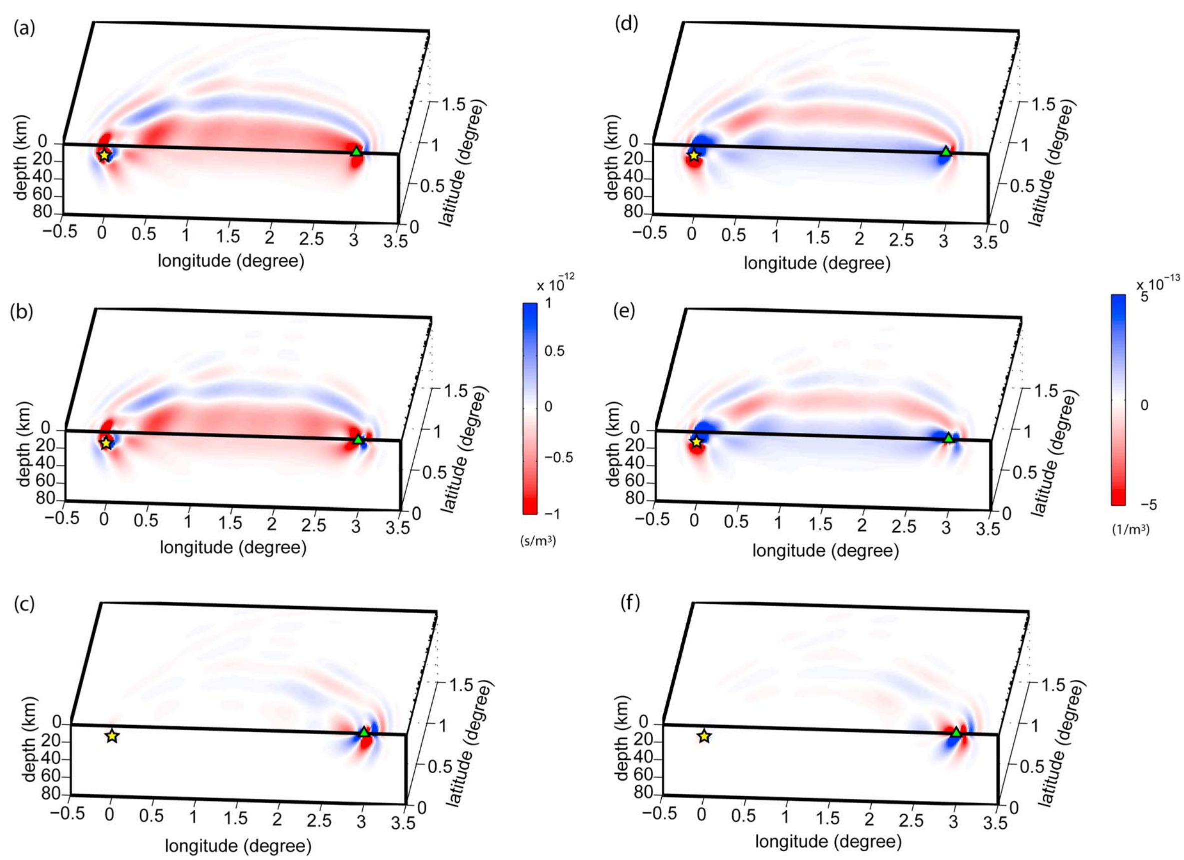

Figure 3. Same as Figure 1 except for the kernels to ρ.

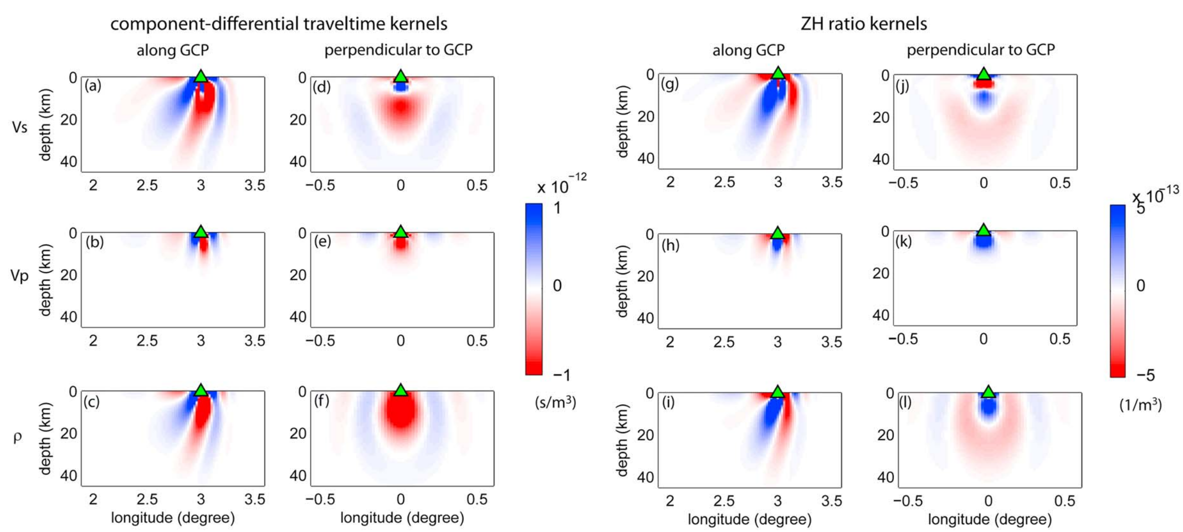

Figure 4. Near-receiver close up views of component-differential traveltime (a–f, the two left columns) and ZH amplitude ratio (g–l, the two right columns) kernels for 10- to 20-s period Rayleigh waves on the vertical profile along the great circle path (a–c and g–i) and the vertical profile perpendicular to the great circle path at the station (d–f and j–l). The green triangle marks the receiver is on the surface. The top subpanels (a, d, g, and j) are the sensitivity to V_s, the middle subpanels (b, e, h, and k) are sensitivities to V_p, and the bottom subpanels (c, f, i, and l) are the sensitivities to ρ, respectively.

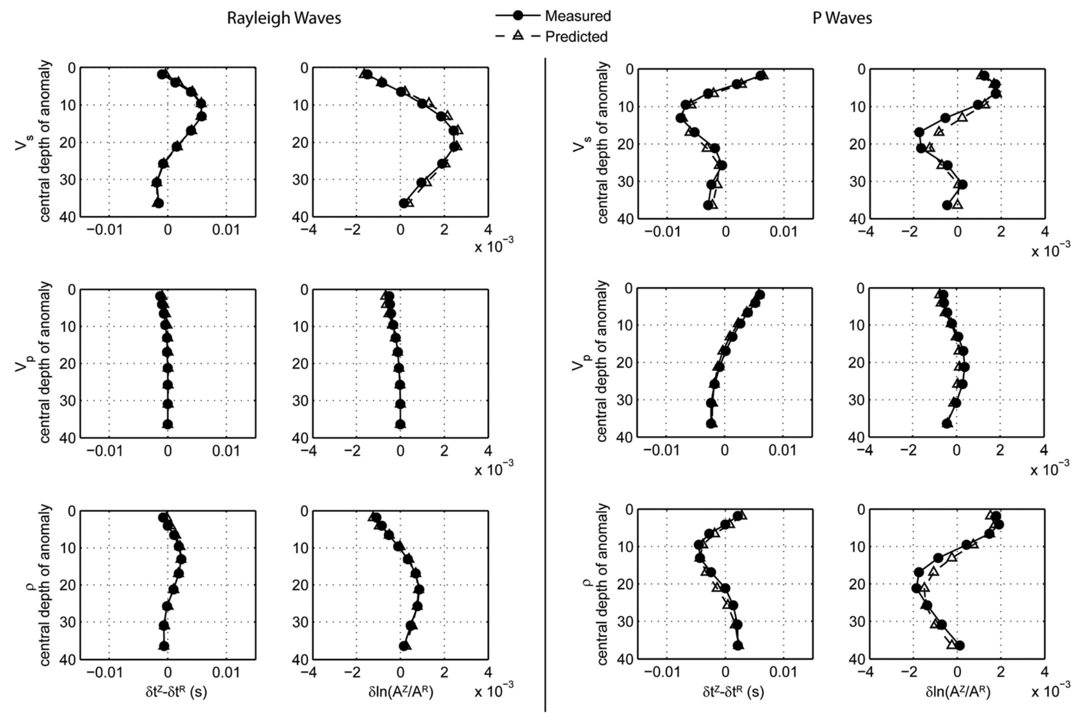

Figure 5. Comparison of the predicted and measured component-differential traveltimes and ZH ratios, respectively, for various central depths of the input anomaly. Columns from left to the right denote Rayleigh wave component-differential traveltimes, Rayleigh wave ZH ratios, *P* wave component-differential traveltimes, and *P* wave ZH ratios. Rows from top to bottom represent the results based on the perturbation of V_s, V_p, and ρ, respectively. The values are for Rayleigh and *P* waves at 10- to 20-s period. Notice that the ZH ratios described in this paper are all in logarithm.

individual periods from 10 to 20 s shows that the reduced 3-D kernels mainly lie within those 1-D kernels. The second source is that these reduced 3-D kernels are calculated from the superposition of fundamental mode and higher modes of Rayleigh waves, while the 1-D kernels shown here only account for the fundamental mode. There is a notable difference between the 3-D and 1-D kernels with respect to V_s at depths greater than 20 km (Figure 6). This reflects the contribution of higher modes in the 3-D kernels. To confirm this, we show in Figure S7 that the negative sensitivity in the V_s kernel below 20 km depth nearly completely disappears when the source is moved from 12.315-km depth to the Earth surface. As the source becomes shallow, higher modes are greatly reduced in amplitude relative to the fundamental mode (Forsyth, 1976; Harkrider & Anderson, 1966), resulting in a large reduction in the contribution of the higher modes to waveforms and thus the kernels.

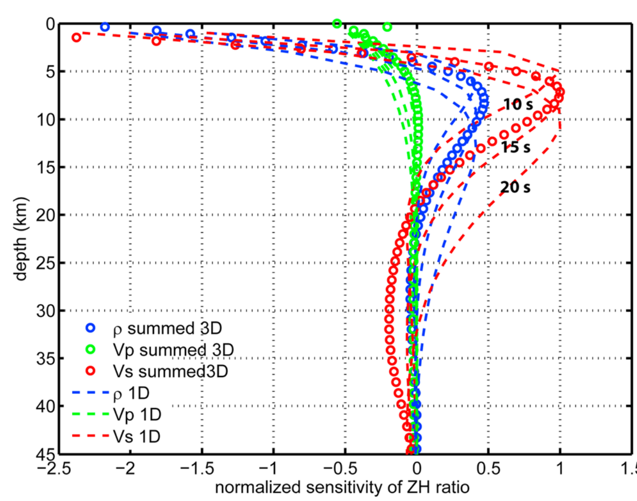

Figure 6. Comparison of the 1-D ZH ratio kernels at 10-, 15-, and 20-s periods (dashed lines) and laterally summed, reduced 3-D ZH ratio kernels at 10- to 20-s periods (circles).

In section 4.1, we provided an example of how the component-differential traveltimes and ZH ratios at a station vary with the structural perturbation at various depths and 20 km away from the station (Figure S4). In theory, 1-D ZH ratio kernels represent the sensitivity to structures only beneath a station, so the 1-D kernels would predict zero component-differential traveltime or ZH ratios at the

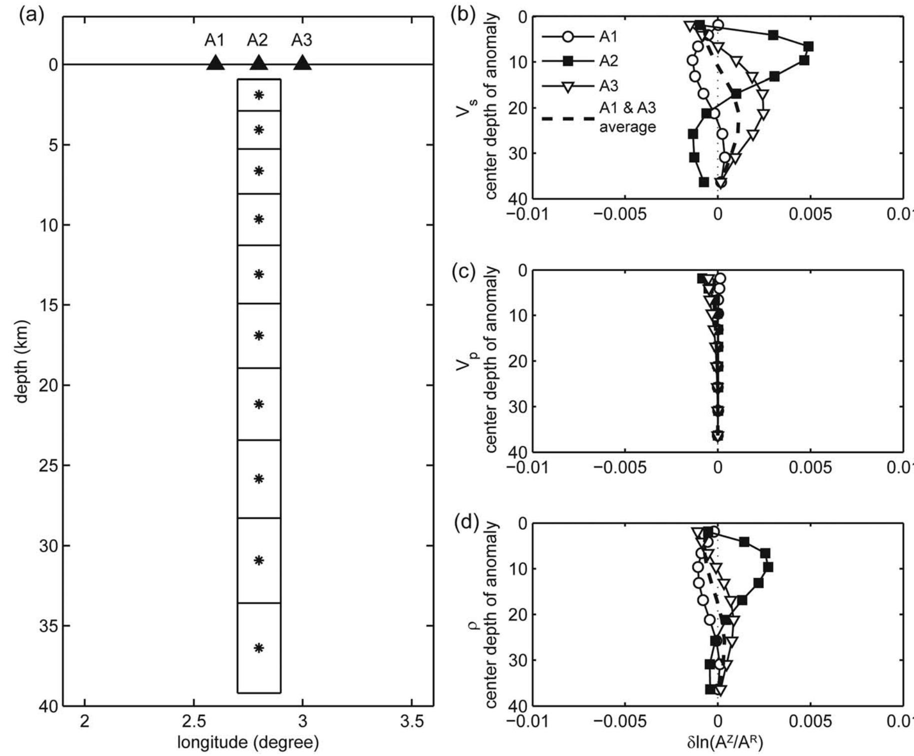

Figure 7. A series of synthetic tests to demonstrate the sensitivity of the ZH ratios to the 3-D structures near the stations. (a) The geometry of the stations and model perturbation. See text in section 4.1 for details about the model perturbation. The three stations A1, A2, and A3 are located on the surface along a great circle path from the source at (0°, 0°). The central station A2 is at (0°, 2.8°E), right above the centers of the perturbation; the other two stations are at (0°, 2.6°E) and (0°, 3°E), respectively. Each synthetic test is carried out for a perturbation outlined by a box with an asterisk at the center. Together these tests produce the measured ZH ratios for V_s, V_p, or ρ perturbations shown in (b)–(d), respectively. Dashed lines in (b)–(d) show the average of the ZH ratios measured at A1 and A3 for given depths. Symbols are consistent in (b)–(d).

station, contradicting with the measured component-differential traveltimes and ZH ratios from full-wave simulation (Figure 5). As an inverse problem, the 1-D kernels would erroneously map the measured anomalies caused by a perturbation 20 km away to right beneath the station.

In practice, ZH ratio measurements were averaged over back azimuths (Berbellini et al., 2017; Tanimoto & Rivera, 2008). Smoothing techniques such as isotropic Gaussian smoothing were also applied in inversion based on 1-D ZH ratio kernels (e.g., Lin et al., 2012; Workman et al., 2017). Those treatments make the averaged ZH ratio more compatible with the 1-D kernels, suppressing the sensitivity of the ZH ratios to the 3-D structure near the station. To further illustrate this, we apply the same structural perturbation as in section 4.1 then measure and compare the ZH ratios of the simulated waveforms at three stations evenly separated by about half wavelength along the great circle path: The same station as in section 4.1, a central station right above the perturbation, and the third one 0.2° before the perturbation (Figure 7). We find that the ZH ratios at the three stations reach their peaks at different depths, reflecting different depth sensitivities at different lateral distances from the velocity perturbation. For the perturbation within a certain depth range (e.g., ~20 km in Figure 7), the ZH ratio at the central station A2 can be much smaller than those at the station A3 (the same station as in Figures 1–6) at a farther epicentral distance. We also notice that the ZH ratios at the two outer stations (A1 and A3) are not antisymmetric and thus cannot be fully canceled by lateral (i.e., back azimuthal) summation or smoothing, as shown as the dashed lines in Figure 7.

We also calculate the back azimuthally averaged 3-D kernels for station A3 (Figure S8). One major feature in these azimuthally averaged kernels is the axisymmetric pattern with respect to the station at any given depth. This result generally agrees with Maupin (2017). However, unlike the true 3-D kernels, which have significant sensitivities extending to ~40 km depth (Figure 4), the back azimuthally averaged sensitivity becomes very small below 20 km depth, which is consistent with the pattern of the 1-D kernel and the laterally summed

10.1029/2017JB015421

3-D kernel as shown in Figure 4. This is because the positive and negative values in the true 3-D kernels are nearly canceled out at greater depths with back azimuthal averaging.

To assess the dependence of the 3-D ZH kernels to the reference model and 3-D velocity structure, we modified the reference model with a uniform 5% V_s change within a 0.2° wide and 5 km thick rectangular prism below the station located at (0°, 3°) and calculated the 3-D ZH kernels for the perturbed model. A comparison of the kernels before and after the model perturbation shows that the largest change in the kernels is located near the surface above the block in which V_s is perturbed (Figure S9). The bulk change in the absolute values of the kernels, defined as $\sum|K_1|/\sum|K_0| - 1$ in percentage, is 1.6% for the V_s kernel, 2.4% for the V_p kernel, and 1.4% for the ρ kernel. This change is of the same magnitude of change in velocity, highlighting the importance of iterative updating the 3-D velocity model and sensitivity kernels in inversion for studies where there are substantial 3-D velocity variations.

Our analyses indicate that although the 1-D kernels are adequate for laterally smooth and large-scale (greater than one wavelength) structures, 3-D full-wave kernels based on 3-D reference velocity models are more accurate in predicting ZH ratios affected by small-scale velocity variations near the station. For dense seismic arrays, defined as having station spacing less than one wavelength and thus overlapping 3-D ZH ratio kernels, the 3-D kernels as presented in this study have the potential to significantly improve the resolution of fine structures.

4.3. Trade-Off Between V_s and ρ in Using 3-D Kernels

The strong sensitivity of ZH ratios and component-differential traveltimes with respect to ρ indicates that the resulting V_s model from those observables can be significantly biased if the density structure is not accounted for in inversion. However, the similar patterns of the component-differential kernels with respect to V_s and ρ (Figures 4 and 6) suggest strong trade-off between these two parameters in the component-differential observables. In order to reduce this trade-off, a common practice in seismic tomography is to employ the a priori empirical relationship of V_s~ρ (e.g., Moulike & Ekström, 2016), as well as V_p~ρ if V_p is also solved in inversion (e.g., Brocher, 2005; Christensen & Mooney, 1995). A caveat of this practice is that the velocity-density relation varies substantially with rock types (Gardner et al., 1974), so the empirical relationships are likely not universally applicable. There are also times when independent estimates of the density and velocity are key to geological interpretations, so they need to be determined separately from observations. One possible approach to reduce the density-velocity trade-off is a joint inversion of the component-differential observables and gravity data, which can provide independent constraints on lateral density variations, for both the velocity and density. Incorporation of ZH ratios and component-differential traveltimes of *P* waves (Figures 4 and S10) as well as other seismic measurements (e.g., surface wave phase velocity and receiver functions) in a joint inversion may also help reduce the trade-off between V_s and ρ in the resulting model as they provide different constraints on the velocity and density structures.

5. Conclusion

Using finite difference modeling of wave propagation in 3-D structures and the scattering-integral method, we calculate 3-D sensitivity kernels of Rayleigh and *P* wave differential traveltime on the vertical and radial components and ZH amplitude ratio to V_s, V_p, and density perturbations. The kernels for a simple uniform velocity and density model are presented to illustrate their highly 3-D nature. The differential kernels are significant only near the receiver over an area of approximately one wavelength. Unlike the 1-D depth sensitivity kernels, our 3-D sensitivity kernels vary with azimuths and distances to the receiver, as well as with depth, indicating resolving power in both lateral and vertical directions. The 3-D sensitivity kernels are validated by comparing the predictions from the kernels with the measurements from numerical simulations of wave propagation with various small-scale perturbations in the model. By laterally summing up the 3-D sensitivity kernels, we verify the similarity of the reduced kernels to the 1-D depth sensitivity kernels based on the same model. The small differences between the two are attributed to (1) the finite period range of the 3-D kernels versus the single period of the 1-D kernels and (2) the waveforms used to calculate the 3-D kernels involve both fundamental-mode and higher-mode Rayleigh waves, while the 1-D kernels are only for the fundamental mode. Our results indicate that both the Rayleigh and body wave ZH ratios and component-differential traveltimes provide constraints on the structure near the station. The overall good match between the 1-D kernels and the reduced 3-D full-wave kernels suggests that the traditional approaches based on 1-D kernels is a cost-effective tool to image structures larger than approximately one wavelength. But at finer scales, our 3-D full-wave kernels can be a powerful tool to invert for high-resolution velocity and density tomographic models in places of seismic arrays with station spacing less than one wavelength. In a subsequent study, we will investigate how these kernels can be used with and without other constraints (e.g., gravity, Rayleigh wave phase velocities, and receiver functions).

Acknowledgments
We gratefully acknowledge Victor Tsai, Toshiro Tanimoto, and an Associate Editor for their constructive comments. We thank Huajian Yao for providing the code to calculate the 1-D sensitivity kernels of ZH ratios. Xueyang Bao and Yang Shen are supported by Air Force Research Laboratory (contract FA9453-16C-0019). Simulations were performed using a finite-difference code cited in the references. The paper is theoretical and no observed data are used.

References

Aki, K., & Richards, P. G. (1980). *Quantitative seismology: Theory and methods*. San Francisco, CA: W. H. Freeman & Co.

Attanayake, J., Ferreira, A. M. G., Berbellini, A., & Morelli, A. (2017). Crustal structure beneath Portugal from teleseismic Rayleigh wave ellipticity. *Tectonophysics*, *712-713*, 344–361. https://doi.org/10.1016/j.tecto.2017.06.001

Berbellini, A., Morelli, A., & Ferreira, A. M. G. (2017). Crustal structure of northern Italy from the ellipticity of Rayleigh waves. *Physics of the Earth and Planetary Interiors*, *265*, 1–14. https://doi.org/10.1016/j.pepi.2016.12.005

Boore, D., & Toksöz, M. N. (1969). Rayleigh wave particle motion and crustal structure. *Bulletin of the Seismological Society of America*, *59*, 331–346.

Brocher, T. M. (2005). Empirical relations between elastic wavespeeds and density in the Earth's crust. *Bulletin of the Seismological Society of America*, *95*(6), 2081–2092. https://doi.org/10.1785/0120050077

Chen, P., Jordan, T. H., & Zhao, L. (2007). Full three-dimensional tomography: A comparison between the scattering-integral and adjoint-wavefield methods. *Geophysical Journal International*, *170*(1), 175–181. https://doi.org/10.1111/j.1365-246X.2007.03429.x

Chong, J., Ni, S., Chu, R., & Somerville, P. (2016). Joint inversion of body-wave receiver function and Rayleigh-wave ellipticity. *Bulletin of the Seismological Society of America*, *106*(2), 537–551. https://doi.org/10.1785/0120150075

Chong, J., Ni, S., & Zhao, L. (2015). Joint inversion of crustal structure with the Rayleigh wave phase velocity dispersion and the ZH ratio. *Pure and Applied Geophysics*, *172*(10), 2585–2600. https://doi.org/10.1007/s00024-014-0902-z

Christensen, N. I., & Mooney, W. D. (1995). Seismic velocity structure and composition of the continental crust: A global view. *Journal of Geophysical Research*, *100*(B6), 9761–9788. https://doi.org/10.1029/95JB00259

Ferreira, A. M. G., & Woodhouse, J. H. (2007). Observations of long period Rayleigh wave ellipticity. *Geophysical Journal International*, *169*(1), 161–169. https://doi.org/10.1111/j.1365-246X.2006.03276.x

Fichtner, A. (2011). *Full seismic waveform modeling and inversion*. Berlin, Heidelberg: Springer-Verlag. https://doi.org/10.1007/978-3-642-15807-0.

Forsyth, D. W. (1976). Higher-mode Rayleigh waves as an aid to seismic discrimination. *Bulletin of the Seismological Society of America*, *66*(3), 827–841.

Gardner, G. H. F., Gardner, L. W., & Gregory, A. R. (1974). Formation velocity and density—Thediagnostic basics for stratigraphic traps. *Geophysics*, *39*(6), 770–780. https://doi.org/10.1190/1.1440465

Gouédard, P., Seher, T., McGuire, J. J., Collins, J. A., & van der Hilst, R. D. (2014). Correction of ocean-bottom seismometer instrumental clock errors using ambient seismic noise. *Bulletin of the Seismological Society of America*, *104*(3), 1276–1288. https://doi.org/10.1785/0120130157

Hannemann, K., Krüger, F., & Dham, T. (2014). Measuring of clock drift rates and static time offsets of ocean bottom stations by means of ambient noise. *Geophysical Journal International*, *196*(2), 1034–1042. https://doi.org/10.1093/gji/ggt434

Harkrider, D. G., & Anderson, D. L. (1966). Surface wave energy from point sources in plane layered Earth models. *Journal of Geophysical Research*, *71*(12), 2967–2980. https://doi.org/10.1029/JZ071i012p02967

Li, G., Chen, H., Niu, F., Guo, Z., Yang, Y., & Xie, J. (2016). Measurement of Rayleigh wave ellipticity and its application to the joint inversion of high-resolution *S* wave velocity structure beneath northeast China. *Journal of Geophysical Research: Solid Earth*, *121*, 864–880. https://doi.org/10.1002/2015JB012459

Lin, F.-C., Schmandt, B., & Tsai, V. C. (2012). Joint inversion of Rayleigh wave phase velocity and ellipticity using USArray: Constraining velocity and density structure in the upper crust. *Geophysical Research Letters*, *39*, L12303. https://doi.org/10.1029/2012GL052196

Lin, F.-C., Tsai, V. C., & Schmandt, B. (2014). 3-D crustal structure of the western United States: Application of Rayleigh-wave ellipticity extracted from noise cross-correlations. *Geophysical Journal International*, *198*(2), 656–670. https://doi.org/10.1093/gji/ggu160

Liu, K., & Zhou, Y. (2016). Travelling-wave Green tensor and near-field Rayleigh-wave sensitivity. *Geophysical Journal International*, *205*(1), 134–145. https://doi.org/10.1093/gji/ggv564

Maupin, V. (2017). 3-D sensitivity kernels of the Rayleigh wave ellipticity. *Geophysical Journal International*, *211*(1), 107–119. https://doi.org/10.1093/gji/ggx294

Moulike, P., & Ekström, G. (2016). The relationships between large-scale variations in shear velocity, density, and compressional velocity in the Earth's mantle. *Journal of Geophysical Research: Solid Earth*, *121*, 2737–2771. https://doi.org/10.1002/2015JB012679

Muir, J. B., & Tsai, V. C. (2017). Rayleigh-wave H/V via noise cross correlation in Southern California. *Bulletin of the Seismological Society of America*, *107*(5), 2021–2027. https://doi.org/10.1785//0120170051

Ritsema, J., Tivera, L. A., Komatitsch, D., Tromp, J., & van Heijst, H. J. (2002). Effects of crust and mantle heterogeneity on PP/P and SS/S amplitude ratios. *Geophysical Research Letters*, *29*(10), 1430. https://doi.org/10.1029/2001GL013831

Shen, Y., Zhang, Z., & Zhao, L. (2008). Component-dependent Fréchet sensitivity kernels and utility of three-component seismic records. *Bulletin of the Seismological Society of America*, *98*(5), 2517–2525. https://doi.org/10.1785/0120070283

Tanimoto, T., & Alvizuri, C. (2006). Inversion of the HZ ratio of microseisms for *S*-wave velocity in the crust. *Geophysical Journal International*, *165*(1), 323–335. https://doi.org/10.1111/j.1365-246X.2006.02905.x

Tanimoto, T., & Rivera, L. (2008). The ZH ratio method for long-period seismic data: Sensitivity kernels and observational techniques. *Geophysical Journal International*, *172*(1), 187–198. https://doi.org/10.1111/j.1365-246X.2007.03609.x

Tanimoto, T., & Tsuboi, S. (2009). Variational principle for Rayleigh wave ellipticity. *Geophysical Journal International*, *179*(3), 1658–1668. https://doi.org/10.1111/j.1365-246X.2009.04360.x

Tanimoto, T., Yano, T., & Hakamata, T. (2013). An approach to improve Rayleigh-wave ellipticity estimates from seismic noise: Application to the Los Angeles Basin. *Geophysical Journal International*, *193*(1), 407–420. https://doi.org/10.1093/gji/ggs123

Tromp, J., Tape, C., & Liu, Q. (2005). Seismic tomography, adjoint methods, time reversal and banana-doughnut kernels. *Geophysical Journal International*, *160*(1), 195–216. https://doi.org/10.1111/j.1365-246X.2004.02453.x

Workman, E., Lin, F.-C., & Koper, K. D. (2017). Determination of Rayleigh wave ellipticity across the Earthscope transportable Array using single-station and array-based processing of ambient seismic noise. *Geophysical Journal International*, *208*(1), 234–245. https://doi.org/10.1093/gji/ggw381

Yano, T., Tanimoto, T., & Rivera, L. (2009). The ZH ratio method for long-period seismic data: Inversion for *S*-wave velocity structure. *Geophysical Journal International*, *179*(1), 413–424. https://doi.org/10.1111/j.1365-246X.2009.04293.x

Yuan, Y., Yao, H., & Qin, Y. (2016). Joint inversion of Rayleigh wave vertical-horizontal amplitude ratios and dispersion based on the neighborhood algorithm and its application (in Chinese with English Abstract). *Chinese Journal of Geophysics*, *59*, 959–971. https://doi.org/10.6038/cjg20160318

Zhang, W., Shen, Y., & Zhao, L. (2012). Three-dimensional anisotropic seismic wave modelling in spherical coordinate by a collocated-grid finite-difference method. *Geophysical Journal International*, *188*(3), 1359–1381. https://doi.org/10.1111/j.1365-246X.2011.05331.x

Zhang, Z., & Shen, Y. (2008). Cross-dependence of finite-frequency compressional waveforms to shear seismic wave speeds. *Geophysical Journal International*, *174*(3), 941–948. https://doi.org/10.1111/j.1365-246X.2008.03840.x

Zhao, L., Jordan, T. H., Olsen, K. B., & Chen, P. (2005). Fréchet kernels for imaging regional Earth structure based on three-dimensional reference models. *Bulletin of the Seismological Society of America*, *95*(6), 2066–2080. https://doi.org/10.1785/0120050081

Zhou, Y., Dahlen, F., & Nolet, G. (2004). Three-dimensional sensitivity kernels for surface wave observables. *Geophysical Journal International*, *158*(1), 142–168. https://doi.org/10.1111/j.1365-246X.2004.02324.x